J Mater Sci (2021) 56:19651–19662

Energy materials

Novel dual-phase symmetrical electrode materials for protonic ceramic fuel cells

Hao Ni[1], Yang Yang[1], Yunfeng Tian[1], Xinxin Wang[1], Shuanglin Shen[2], Keqing Zheng[2], Majid Khan[3], Shaorong Wang[4], and Yihan Ling[1,4,*]

[1] School of Materials Science and Physics, China University of Mining and Technology, Xuzhou 221116, People's Republic of China
[2] School of Electrical and Power Engineering, China University of Mining and Technology, Xuzhou 221116, People's Republic of China
[3] Department of Physics, Abdul Wali Khan University Mardan, Mardan 23200, Pakistan
[4] Jiangsu Province Engineering Laboratory of High Efficient Energy Storage Technology and Equipments, China University of Mining and Technology, Xuzhou 221116, People's Republic of China

Received: 20 May 2021
Accepted: 13 September 2021
Published online: 1 October 2021

ABSTRACT

Protonic ceramic fuel cells (PCFCs) can use hydrogen and hydrocarbon fuels to generate electricity with good performance and anti-cooking resistance. Herein, a novel dual-phase perovskite oxide $BaCe_{0.5}Fe_{0.4}Ni_{0.1}O_{3-\delta}$ (BCFN) with $BaCe_{0.5}Fe_{0.5}O_{3-\delta}$ (BCF) as one reference was synthesized, characterized and then evaluated as the symmetrical electrodes for PCFCs. Both BCF and BCFN can be self-assembled into an orthorhombic cerium-rich oxide phase and a cubic iron-rich oxide phase after calcined at 1000 °C and show good redox stability. BCFN shows much better electrical conductivity and lower area specific resistance than BCF. Applying BCF and BCFN as symmetrical electrodes for PCFCs with the $BaZr_{0.1}Ce_{0.7}Y_{0.2}O_{3-\delta}$ (BZCY) electrolyte supporting, the cell performance with BCFN symmetrical electrode is almost twice (141 $mW{\cdot}cm^2$ at 700 °C) than those with BCF symmetrical electrode, and the electrode polarization resistances are also reduced from 0.7 to 0.5 $\Omega{\cdot}cm^2$ using humidified H_2. The preliminary experimental results can demonstrate that dual-phase perovskite oxides with nanoparticle in situ precipitation are very promising symmetrical electrodes for protonic ceramic fuel cells.

Handling Editor: Mark Bissett.

Address correspondence to E-mail: lyhyy@mail.ustc.edu.cn; lyhyy@cumt.edu.cn

https://doi.org/10.1007/s10853-021-06531-8

Introduction

Symmetrical solid oxide fuel cells (SSOFCs) possess a unique configuration by applying the same anode and cathode materials, which can greatly simplify the fabrication technology and improve the thermomechanical compatibility between each component [1–4]. More importantly, the carbon deposition and sulfur poisoning problems faced by the traditional Ni-based cermet anode can be eliminated by the utilization of SSOFCs configuration. Because the air and fuel gas flow can be reversed owing to the same electrode material, thus the carbon and sulfur particles can be removed [5, 6]. At present, the relatively mature SSOFCs usually use high temperature oxygen ion conductors YSZ or LSGM as electrolyte materials due to their good stability and mechanical property. However, their ionic conductivity is greatly limited at low temperature. For example, SSOFCs with YSZ electrolyte generally operate at over 800 °C in order to reduce the ohmic resistance [7–9].

With the aim to maintain the benefits of SSOFCs at reduced working temperature, symmetrical protonic ceramic fuel cells (PCFCs) have come into people's attention [10, 11]. PCFCs using a proton conducting material as electrolyte and working at 500–700 °C, which have been regarded the one of the most suitable electrochemical devices for energy conversion owing to the high energy efficiency and low activation energy. Compared with the conventional oxygen ion conducting configuration, the production of PCFC (steam) is generated at the cathode side and will not dilute the fuel gas [12]. However, since there is no oxygen ion supplied to anode side of PCFC, excessive carbon monoxide may lead to carbon deposition when using hydrocarbon fuels [13, 14]. To overcome this problem, Duan et al. proposed the anti-coking mechanism of protonic nickel-based cermet anode under the action of hydrogen and oxygen ions, and achieved the outstanding durability at 600 °C in a variety of hydrocarbon fuels [15]. A large amount of steam is provided and participated the fuels reforming processes, as shown in Fig. 1. The mainly reactions occurred at the anode side of PCFC when using ethanol fuel can be expressed as follows:

$$CH_3CH_2OH + 3H_2O = 2CO_2 + 12H^+ + 12e^- \quad (1)$$

$$CO + H_2O = CO_2 + 2H^+ + 2e^- \quad (2)$$

The high temperature and exothermic oxidation at SOFC anode are not conducive to the forward water–gas shift (2) and will cause the accumulation of CO [16, 17]. Conversely, the low-temperature and endothermic nature of steam reforming in PCFC can further promote the conversion of CH_3CH_2OH to H_2 due to the continuously removable proton from the anode (1) and thus not limited by thermodynamic equilibrium [18, 19]. In addition, the steam reformation reaction of PCFC at low temperature also contributes to the formation of a low CO/CO_2 ratio, which hinders the forward progress of the Boudouard reaction and improves the coking tolerance [20].

Ni-based cermet are normally used as anode material for PCFCs. However, Ni-based anodes are prone to the carbon deposition reactions [13, 21]. Recently, perovskite oxide materials have been widely investigated to replace the conventional Ni-based anode owing to their good coking tolerance and good redox cycle stability [22]. However, the lack of metal active centers results in poor catalytic activity and larger anode polarization [23, 24]. $BaFeO_{3-\delta}$ (BFO) is a promising parent oxide for SOFC cathodes [25, 26]. The transition metal Fe has variable oxidation and spin states, which potentially contribute high catalytic activity and strong resistance in cathode environment. Meanwhile, the large ionic radius and relatively low divalent state of Ba^{2+} is favorable toward the creation of more free lattice volume and oxygen vacancies for oxygen transport. Tao et al. have proposed a kind of multiphase composite cathode for PCFC [27]. The precursor $BaCe_{0.5}Fe_{0.5}O_{3-\delta}$ (BCF) decomposes at high temperature into two uniformly dispersed and stable perovskite oxides: the main proton conductor phase $BaCe_{0.85}Fe_{0.15}O_{3-\delta}$ (BCF8515) and the main electronic conductor phase $BaCe_{0.15}Fe_{0.85}O_{3-\delta}$ (BCF). The transportation of protons and electrons in the two phases greatly increases the conductivity and enlarges the three phases boundary. Recently, Chen et al. found that the BCF ceramic membrane shows an extremely high hydrogen permeation flux [28]. Considering the good proton conductivity of iron-doped $BaCeO_3$ system and the low coking tolerance of Ni-cermet anode, $BaCe_{0.5}Fe_{0.5}O_{3-\delta}$ (BCF) was synthesized and evaluated as the symmetrical electrode material for PCFCs based on $BaZr_{0.1}Ce_{0.7}Y_{0.2}O_{3-\delta}$ (BZCY) electrolyte. In

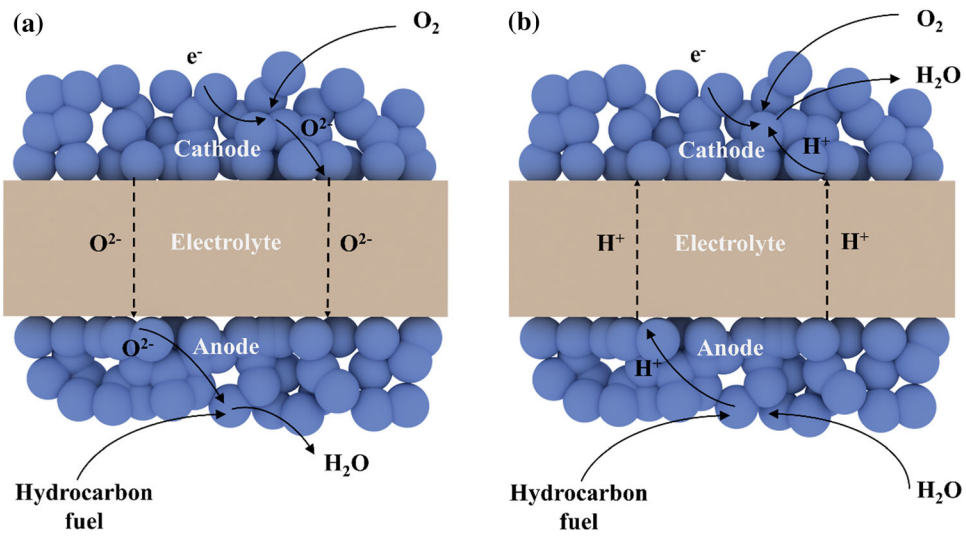

Figure 1 Comparison of **a** oxygen ion conductor SSOFC and **b** proton conductor SSOFC.

order to further enhance the catalytic activity, Ni was introduced to BCF ($BaCe_{0.5}Fe_{0.4}Ni_{0.1}O_{3-\delta}$, BCFN). The electrochemical performance of the modified symmetrical electrode was systematically investigated.

Experimental

Powder synthesis

$BaCe_{0.5}Fe_{0.5}O_{3-\delta}$ and $BaCe_{0.5}Fe_{0.4}Ni_{0.1}O_{3-\delta}$ powders were prepared by EDTA-citrate combustion method. Dissolving the stoichiometric proportion of $(CH_3COO)_2Ba$, $Ce(NO_3)_3{\cdot}6H_2O$, $Fe(NO_3)_3{\cdot}9H_2O$ and $Ni(NO_3)_2{\cdot}6H_2O$ in distilled water. Followed by adding nitric acid for combustion-supporting, citric acid and EDTA as complexing agent. Then the PH value was adjusted to 7 by ammonia. After stirring and heating in evaporating dish, the clear solution gradually became viscous gel and then self-sustaining combustion occurred, resulting in light yellow ash. The ashes were calcinated at 1000 °C for 3 h to obtain the pure phase of BCF and BCFN powders. The electrolyte powders of BZCY were also synthesized using the EDTA-citrate combustion method and calcined at 1000 °C for 3 h.

Cell fabrication

The calcined BZCY powders were milled with zirconia balls in ethanol for 12 h. After drying at 70 °C, the BZCY disks with a diameter of 15 mm were fabricated by dry-pressing technology and sintered at 1400 °C for 5 h to achieve densification. A proper amount of BCF or BCFN powder was mixed with 10% ethyl cellulose–terpineol to prepare electrode ink. Then both sides of the electrolyte disks were painted with the electrode ink. The assemblies were calcined at 1000 °C for 3 h to apply symmetrical cells. And the active area in cathode of the single cell is 0.2 cm^2.

Characterization and cell measurement

The crystal structure of BCF and BCFN powders was characterized by X-ray diffraction (XRD, DX-2800 diffractometer). In order to compete the measurement of conductivity test, the rectangular BCF and BCFN samples ($0.15 \times 0.4 \times 1.4$ mm^3) were pressed and then sintered at 1300 °C to achieve densification. The conductivity of electrode was measured by standard DC four-probe method on a digital multimeter (KEITHLEY 2000). The electrochemical performance of the cells was measured by AC impedance spectroscopy workstation (CHI604E, Shanghai Chenhua) with temperature range from 700 to 600 °C. Current density (I)–Voltage (V)–Powder density (P) curves of cells were measured on electrochemical workstation using humidified hydrogen as fuel with an intake flow of 40 $mL{\cdot}min^{-1}$. The frequency range of EIS was set to 1 MHz ~ 0.01 Hz with voltage amplitude of 10 mV. The long-term testing of single cells was set with a constant voltage of 0.7 V and recorded the data of running for 100 h. Significantly, the stability performance of the cells with BCFN electrodes was measured on another

electrochemical workstation (ZenniumE, Germany) due to the damage on the original instrument. Field emission scanning electron microscopy (SEM) was performed to observe the cross-sectional morphology of single cells.

Results and discussion

Figure 2a shows the XRD patterns of the pre-calcined BCF and BCFN powders. It can be seen that the prepared precursor powders decomposed into a dual-phase compound which consists of an orthorhombic perovskite phase and a cubic perovskite phase after calcining at high temperature, as Tao et al. reported [27]. In addition, the characteristic peaks of corresponding crystal planes of BCF are clearly observed in BCFN samples. This indicates that the substitution of Ni at the B-site does not affect the formation of the dual-phase compound. Typical (110) peak of BCF which originally observed at 30.75° shifts to a higher angle (30.79°) in BCFN owing to the shrinkage of the crystal cell, further illustrating the replacement of iron ions by nickel ions with a smaller radius [29]. The chemical compatibility of BCF and BCFN electrode with BZCY electrolyte was examined after calcined in air for 5 h under a certain temperature gradient. As shown in Fig. 2a, all the peaks assigned to the perovskite phase corresponding to original electrode materials and BZCY,

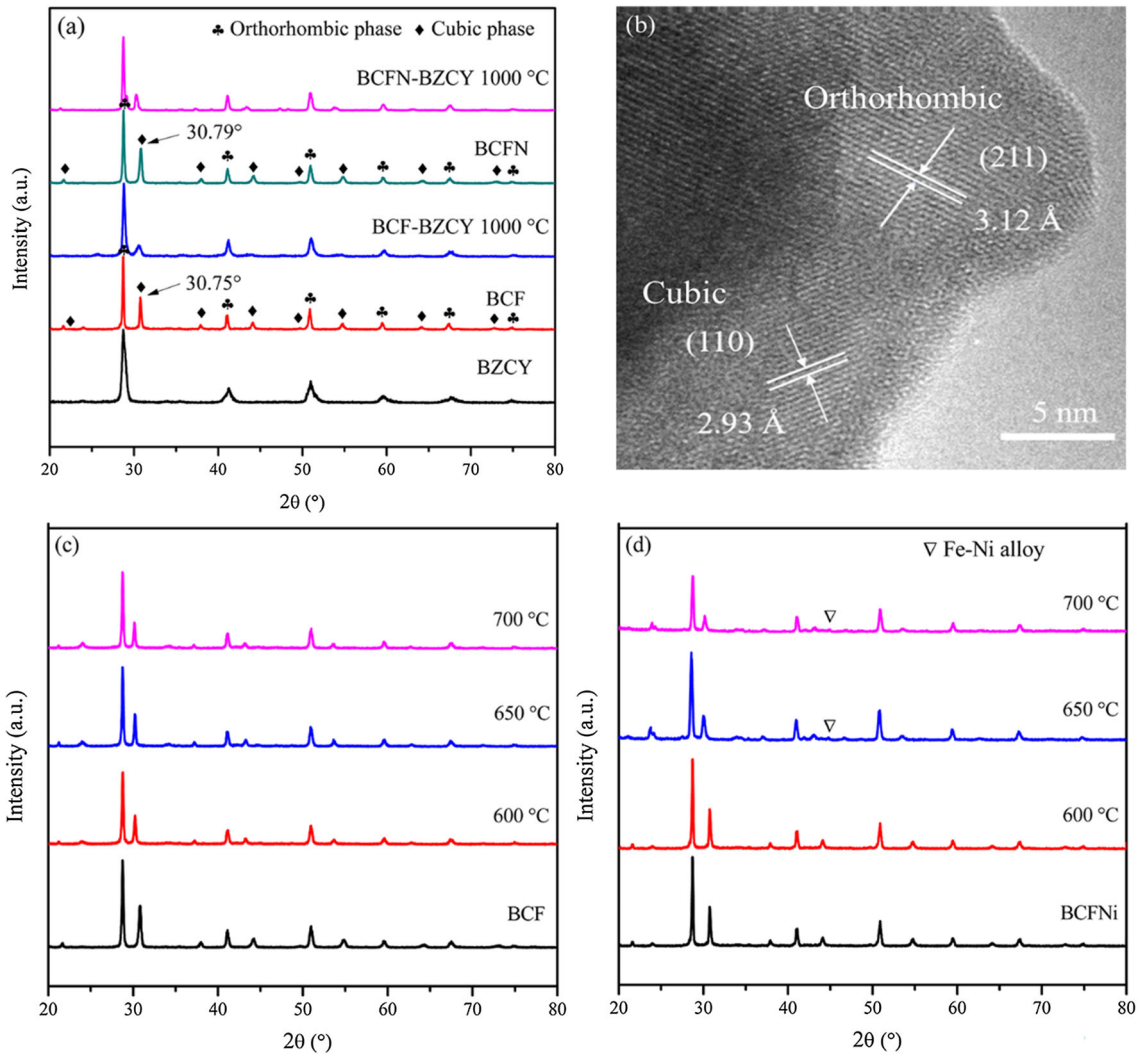

Figure 2 **a** XRD patterns of BCF and BCFN powder calcined at 1000 °C for 3 h and the chemical compatibility between BZCY electrolyte; **b** The typical HR-TEM images of the as-prepared BCFN sample; XRD patterns of as-synthesized **c** BCF and **d** BCFN powder calcined at 1000 °C in air and reduced at different temperature in humidified H_2.

demonstrating good chemical compatibility. It also indicates that cerium in BZCY would not affect the self-assembly behavior of electrode in the cell structure with $BaCO_3$-based perovskite oxide as both electrode material and electrolyte material. The TEM image shown in Fig. 2b confirms the phase structure of BCFN. The characteristic lattice fringe spacing of the (110) crystal plane of BCFN is 2.93 Å, related to the cubic perovskite structure. The spacing of (211) planes is 3.12 Å, corresponding to the orthorhombic perovskite structure.

The phase structure of BCF and BCFN powders treated in humidified H_2 was also investigated by the XRD technology. As shown in Fig. 2c, BCF without Ni doping still exhibits only orthorhombic and cubic phases after being reduced at 700 °C for 5 h, which shows excellent redox stability. However, after substituting the Fe sites with fewer Ni ions, the perovskite phase was effectively weakened in Fig. 2d. Moreover, when the reduction temperature reached 650 °C, the additional Fe–Ni alloy peaks appear between 42° and 45° from the XRD patterns of BCFN [30]. It indicates that the in situ formation of Fe–Ni alloy will occur when the operation temperature is higher than 650 °C in H_2. These exsoluted alloy particles will inevitably improve the catalytic activity of the anode in a reducing atmosphere, thus affecting the electrochemical performance of the electrode and even the single cell [31–33].

Figure 3a shows the electrical conductivity of BCF and BCFN tested from 300 to 800 °C in air. The conductivity shows an upward tendency with the increase of temperature and reaches the maximum value at 550 °C. Then, it becomes to decrease with the further increasing temperature, which has a fairly consistence with the reported results of B-site doped $BaFeO_3$ [34, 35]. The increase of conductivity below 550 °C is attributed to the thermally activated process of small polaron hopping, and the temperature increase significantly promotes the conductivity of BCFN. However, by further increasing the temperature, the formation of oxygen vacancies will accelerate and thus the concentration of electron holes will reduce. Simultaneously, the reduction of high-valent iron ions driven by high temperature will lead to a decrease in carrier concentration [34]. The defect reaction as follows:

$$2Fe_{Fe} + O_O^{\times} \rightarrow \ddot{V}_O + 1/2O_2(g) + 2Fe_{Fe}^{\times} \quad (3)$$

By comparing the data in Fig. 3a, it can be seen that the substitution of Ni significantly improved the conductivity. The conductivity of BCFN is about 1.68 $S{\cdot}cm^{-1}$ at 550 °C, while BCF is only 0.98 S cm^{-1} at the same temperature. The low-valence metal nickel doping inhibits the reduction of iron ions and the generation of oxygen vacancies, and at the same time increases the concentration of electron hole, which leads to the improvement of conductivity:

$$2NiO \rightarrow 2Ni_{Fe}^{'} + \ddot{V}_O + 2O_O^{\times} \quad (4)$$

As shown in Fig. 3b, the conductivity of BCF and BCFN in humidified H_2 (3% H_2O) was also recorded. Unlike the results measured in air, the conductivity of these two samples under hydrogen increases with increasing temperature, showing a thermally activated semiconducting behavior [36]. It is noteworthy that the conductivity in hydrogen atmosphere is much lower than that of air, the conductivities of BCFN at 600 °C are 0.32 $S.cm^{-1}$ in H_2 but 1.62 $S.cm^{-1}$ in air. This is due to the concomitant reduction of

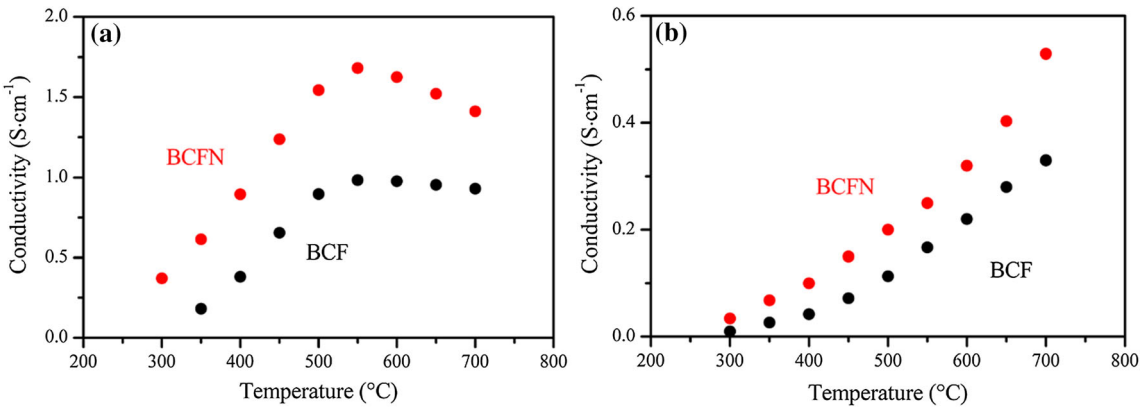

Figure 3 Electrical conductivity of the dense BCF and BCFN sample measured from 300 to 700 °C in **a** air, **b** H_2.

some higher valence cations to lower valence cations to maintain charge neutrality resulted in a decrease in the charge carrier concentration [37]. Similarly, the conductivity in H_2 is also greatly improved by replacing part of Fe with Ni. At 550 °C, the conductivity of BCFN is 0.25 $S{\cdot}cm^{-1}$, which is almost 50% higher than that of undoped BCF (0.17 $S{\cdot}cm^{-1}$).

The impedance spectrum obtained is fitted by an equivalent circuit L-R_1 (R_2-CPE_1) (R_3-CPE_2). Each arc describes a process that leads to the impedance. R1 is the ohmic resistance consist of electrolyte and other cell components. R_2 represents the resistance at high frequency that probably correlated with the transfer of oxygen ions through the electrode/electrolyte interface. R_3 is the resistance at low frequency that may related to the surface oxygen exchange of the electrode [38, 39]. For the convenience of comparison, the ohmic resistance (R_o) of the Nyquist plots is reduced to zero to observe the difference between polarized resistance arcs. Shown in Fig. 4a, the area specific resistance (ASR) of BCFN at 700 °C is 0.067 $\Omega{\cdot}cm^2$ and that of BCF is 0.18 $\Omega{\cdot}cm^2$, demonstrating that the oxygen reduction reaction (ORR) performance is enhanced by doping Ni at Fe site. A similar phenomenon was also observed at lower test temperatures. The BCFN in this work exhibited much outperforming ASR values than other proton conducting cobalt-free cathodes, such as $La_{0.5}Sr_{1.5}MnO_{4+\delta}$- $La_{0.5}Sr_{0.5}MnO_{3-\delta}$ based on BZCY electrolyte (0.34 $\Omega{\cdot}cm^2$ at 700 °C) [40], $Pr_{1.7}Ca_{0.3}NiO_{4+\delta}$-$BaCe_{0.5}Zr_{0.3}Y_{0.2}O_{3-\delta}$ with $BaCe_{0.5}Zr_{0.3}Y_{0.2}O_{3-\delta}$ electrolyte (0.28 $\Omega{\cdot}cm^2$ at 700 °C) [39]. It is also lower than some novel Co contained cathodes, such as $SrCo_{0.4}Fe_{0.15}Zr_{0.05}O_{3-\delta}$ with $BaZr_{0.1}Ce_{0.7}Y_{0.1}Yb_{0.1}O_{3-\delta}$ electrolyte (0.07 $\Omega{\cdot}cm^2$ at 700 °C) [41]. It may due to Ni doping which enhances the conductivity and reduces the charge transfer resistance. The Rp of BCF and BCFN in humidified hydrogen (3% H_2O) was also studied. The results show that BCFN has a lower Rp in all temperature ranges, with recorded values of 0.50, 1.09 and 2.69 $\Omega{\cdot}cm^2$ from 700 to 600 °C, respectively. The decrease in Rp of BCFN indicates that the electrocatalytic oxidation ability can also be improved due to the doping of Ni.

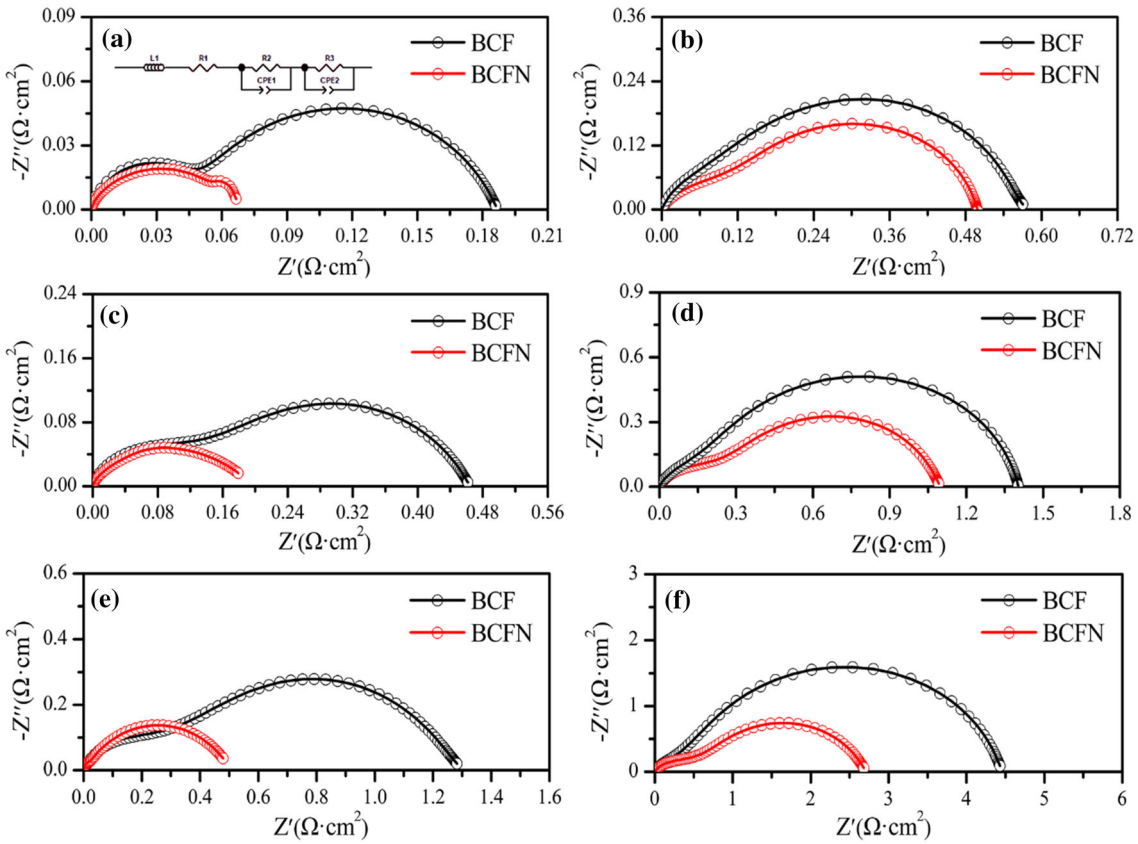

Figure 4 Impedance spectra of BCF and BCFN samples at different temperature in air: **a** 700 °C, **c** 650 °C, **e** 600 °C; and in H_2: **b** 700 °C, **d** 650 °C, **f** 600 °C.

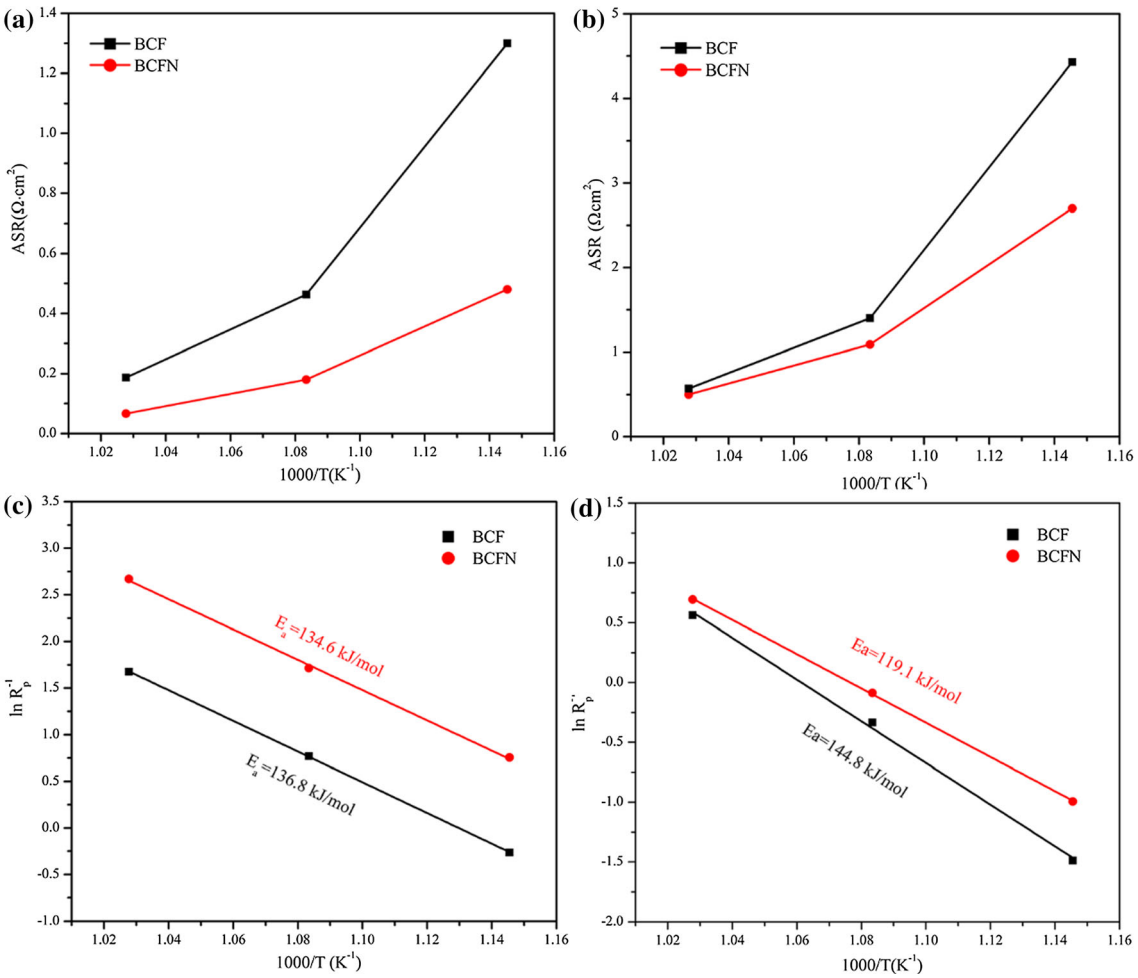

Figure 5 ASR of symmetrical cells with BCF and BCFN as electrodes **a** in air and **b** in H_2; ASR in an Arrhenius diagram as a function of temperature, **c** air and **d** H_2.

Figure 5a–b shows the ASR value of BCF and BCFN from 700 to 600 °C. The change of ASR value with temperature can be intuitively observed. Figure 5c–d shows the Arrhenius plots of the BCF and BCFN in air. The activation energy (E_a) of BCF and BCFN is similar in air. However, the E_a for BCFN cathode is about 1.2 eV in H_2, which is much lower than that of BCF (1.5 eV). The data indicated that BCFN electrode has lower potential barriers of reaction and can achieve higher performance at lower temperatures.

Figure 6a shows the voltage–current density characteristics of BZCY-supported symmetrical cells with BCF electrodes tested using wet H_2 (3% H_2O) as fuel with an intake flow of 40 mL·min^{-1} and air as oxidation from 700 to 600 °C. The open circuit voltage (OCV) with BCFN is 1.085 V at 700 °C, which is slightly improved than BCF (1.076 V) at same temperature. These values are close to the theoretical voltage due to the highly density of BZCY electrolyte. Peak power densities (P_{max}) of 82.7, 60.1 and 28.3 mW·cm^{-2} at 700, 650 and 600 °C were obtained from single cell with BCF electrode, respectively. As shown in Fig. 6b, corresponding P_{max} of single cells with BCFN electrode reached 141, 81.6 and 42.2 mW·cm^{-2} at 700, 650 and 600 °C, respectively, which is almost twice than those with BCF symmetrical electrode. The long-term testing of single cells with BCF and BCFN symmetrical electrode were also measured in H_2 for 100 h as shown in Fig. 6c–d. It can be clearly seen that the current density of both BCF and BCFN cells under test condition for 100 h without obvious degradation, indicating the promising application of BCF and BCFN electrodes in proton conducting SSOFCs. Notably, the abrupt change of the curve at around 60 h in Fig. 6c is due to the

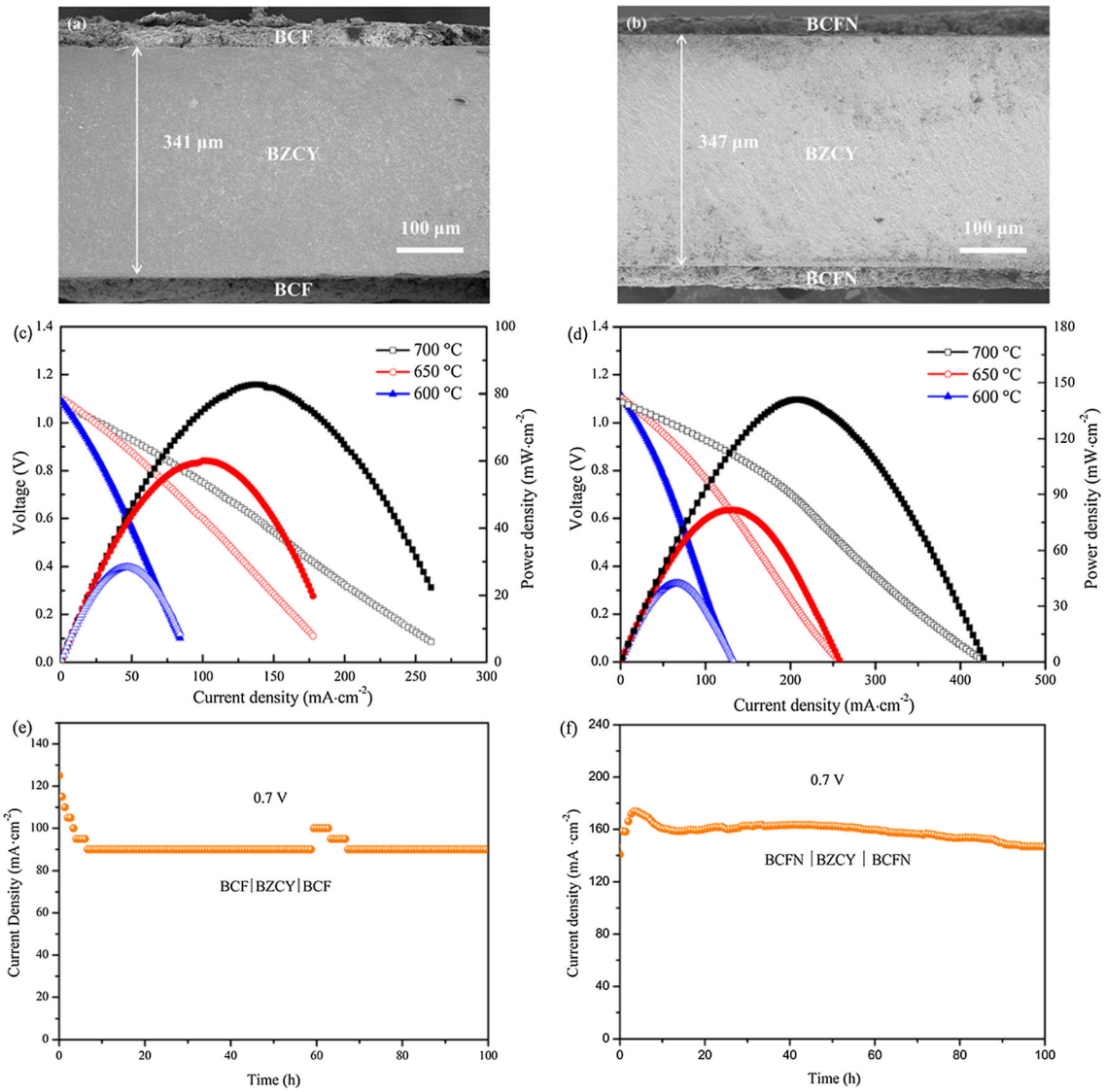

Figure 6 Current–voltage and power density curves of the single cell with **a** BCF, **b** BCFN cathode from 700 to 600 °C. Long-term stability of BZCY-supported single cell with **c** BCF and **d** BCFN symmetrical electrodes.

split of fuels that change the flow rate into the anode chamber. And the whole system tended to be stable after 7 h.

Shown in Fig. 7a–b is the AC impedance spectroscopy of the single cells with BCF and BCFN symmetrical electrodes. The intercept of the spectrum at high frequency and low frequency represents ohmic resistance (R_o) and total resistance (R_t), respectively. The difference between R_t and R_o represents R_p. As shown in Fig. 7a, the Rp of the cell with BCF electrode was 0.7, 1.7, 4.9 Ω·cm^2 at 700, 650 and 600 °C, respectively. And as expected, BCFN exhibited relatively low Rp over the test temperature range with recorded values of 0.5, 1.3 and 3.2 Ω·cm^2 at 700, 650 and 600 °C in Fig. 7b, respectively. It indicates that BCFN is a promising cathode material for proton conducting SSOFCs.

The relaxation time distribution (DRT) method was applied to further elaborate the polarization process of BCFN electrode under SOFC mode, as shown in Fig. 7c. Each deconvolution peak reflects one certain electrochemical process based on the high resolution of DRT method. It has been established that the P1 peak is related to the gas diffusion in porous anode. While P2 and P3 peak are corresponding to the oxygen reduction process and incorporation of O^{2-} in the electrolyte lattice, respectively. The diffusion of protons to the electrolyte surface in anode can be

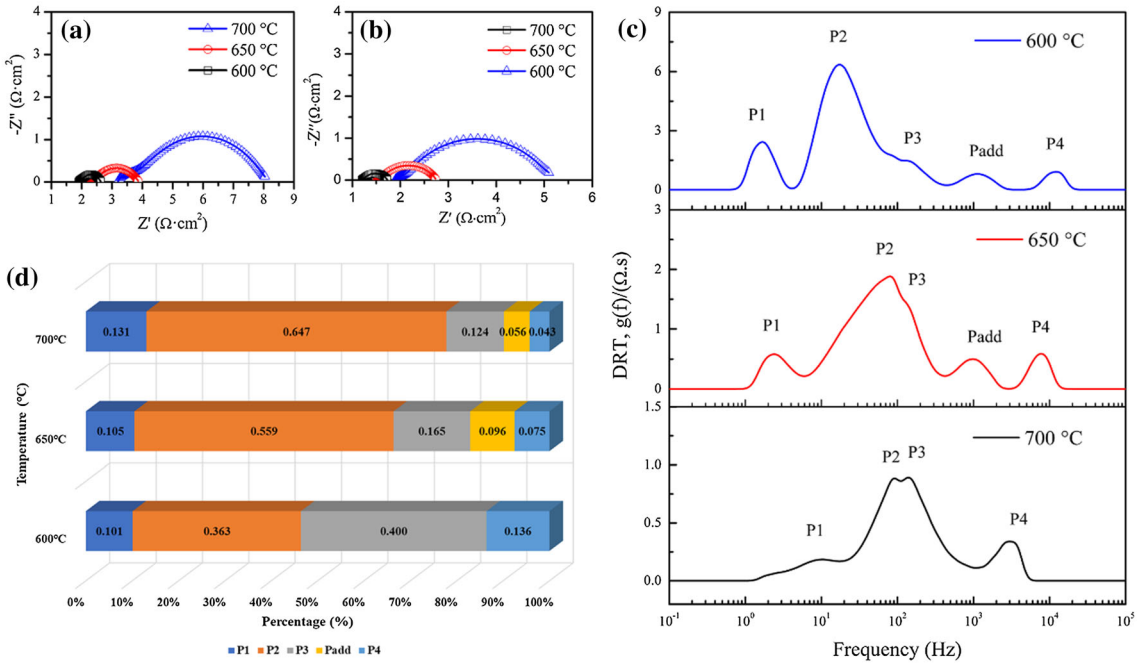

Figure 7 Electrochemical impedance spectra of the single cell with **a** BCF, **b** BCFN symmetrical electrodes; **c** DRT analysis results of BCFN-BZCY-BCFN single cell tested at various temperatures and **d** the proportion of each steps.

represented by P4 [42, 43]. By lowering the test temperature, the rate limiting steps P1-P4 show different trends. The P1, P2 peaks approach the low frequency regions and the P4 peak moves toward high frequencies. In addition, a new polarization peak Padd shows when the temperature drops to 650 °C. The Padd peak represents the hydrogen adsorption/ dissociation process and proton formation reaction on anode [44, 45]. As shown in Fig. 7d, the calculated resistance value of each part at different temperature is expressed as percentages. Obviously, P2 and P3 impedance account for the main proportion of total impedance at 700 °C. As the temperature decreases, the peaks of P2 and P3 gradually separate and the ratio of P2 to P3 increases significantly indicating that the process of oxygen reduction becomes the rate limiting step at lower temperature. As described above, the DRT results reveal that the cathode reaction make a great contribution to the total polarization resistance, which provides a new perspective for further study on the mechanism of proton conducting SSOFC.

The cross-sectional SEM of BCF and BCFN cells after test is shown in Fig. 8. The dense BZCY electrolyte layer is in good contact with the porous electrode layer. And both the BCF and BCFN cathode present a porous structure with inseparably connected particles, which is consistent with the stable ASR value. In addition, BCFN has a smaller grains and finer microstructure than BCF, which is helpful for surface catalytic reaction and ion transport in the electrode. Figure 9 shows the SEM image of the BCFN anode morphology after 100 h of long-term testing. Obviously, plentiful nanoparticles precipitated on the surface of the BCFN anode, and did not destroy the continuous three-dimensional network. According to Fig. 6d, the performance of fuel cell is slightly improved in the first 40 h due to in situ formation of nanoscale particles. Combined with the XRD results in Fig. 2d, it seems that an in situ process of Fe–Ni alloy nanoparticles formation occurs on the BCFN anode. Most of the particles are uniformly dispersed and remain the size of 40 nm although some agglomeration can be seen.

Conclusions

In summary, self-assembled cubic-orthorhombic perovskite nanocomposites with the precursor composition of $BaCe_{0.5}Fe_{0.5}O_{3-\delta}$ and $BaCe_{0.5}Fe_{0.4}Ni_{0.1}O_{3-\delta}$ were prepared and investigated as symmetrical electrodes for PCFC. The transportation of protons and electrons in the two phases greatly increases the

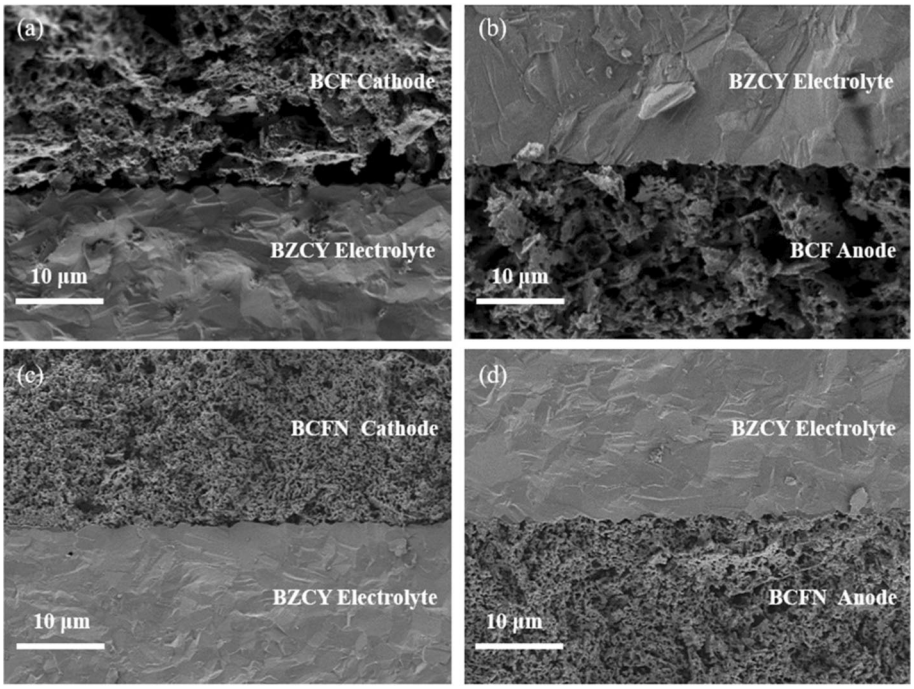

Figure 8 Typical cross-sectional SEM images of the **a**–**b** BCFN and **c**–**d** BCF single cells after test.

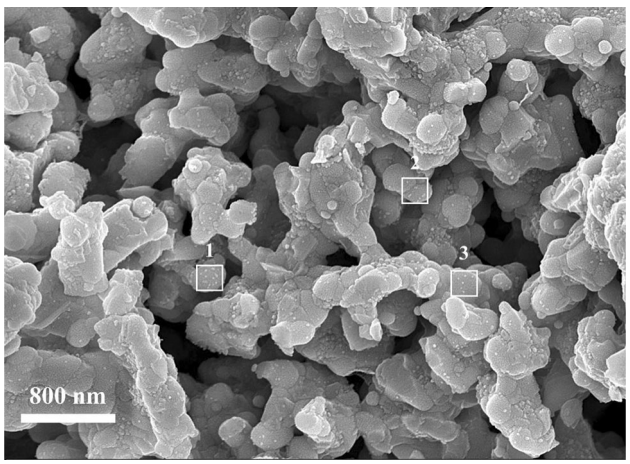

Figure 9 SEM image of anode morphology after long-term testing under hydrogen.

conductivity and enlarges the three phases boundary. The $BaCeO_3$-based electrode and electrolyte materials show good chemical compatibility, which is also the basis for stable long-term operation of the cell. In addition, BCFN shows much better electrical conductivity and lower area specific resistance than BCF, resulting from the partial substitution of Fe with Ni. BCFN exhibits remarkable catalytic activity in air, the ASR of symmetrical cells is only 0.067 $\Omega \cdot cm^{-2}$ at 700 °C. The single cell with BCFN electrode achieves the peak power outputs of 141 $mW \cdot cm^{-2}$ at 700 °C in H_2, which is almost twice than those with BCF symmetrical electrode. The preliminary experimental results can demonstrate that dual-phase perovskite oxides are very promising symmetrical electrodes for protonic ceramic fuel cells.

Acknowledgements

This work was supported by the Ministry of Science and Technology of China (No. 2021YFE0100200), Pakistan Science Foundation (PSF) Project (No. PSF/CRP/18thProtocol (01)), National Natural Science Foundation of China (No. 51806241), China Postdoctoral Science Foundation (No. 2018M632416 and No.2019T120481).

Declarations

Conflict of interest The authors declare that they have no conflict of interest.

References

[1] Bian L, Duan C, Wang L, Zhu L, O'Hayre R, Chou K-C (2018) Electrochemical performance and stability of $La_{0.5}Sr_{0.5}Fe_{0.9}Nb_{0.1}O_{3-\delta}$ symmetric electrode for solid oxide fuel cells. J Power Sources 399:398–405

[2] Ruiz-Morales JC, Canales-Vázquez J, Ballesteros-Pérez B, Peña-Martínez J, Marrero-López D, Irvine JTS, Núñez P

(2007) LSCM–(YSZ–CGO) composites as improved symmetrical electrodes for solid oxide fuel cells. J Eur Ceram Soc 27(13):4223–4227

[3] Vázquez S, Basbus J, Soldati AL, Napolitano F, Serquis A, Suescun L (2015) Effect of the symmetric cell preparation temperature on the activity of $Ba_{0.5}Sr_{0.5}Fe_{0.8}Cu_{0.2}O_{3-\delta}$ as cathode for intermediate temperature solid oxide fuel cells. J Power Sources 274:318–323

[4] Zheng Y, Zhang C, Ran R, Cai R, Shao Z, Farrusseng D (2009) A new symmetric solid-oxide fuel cell with $La_{0.8}Sr_{0.2}Sc_{0.2}Mn_{0.8}O_{3-\delta}$ perovskite oxide as both the anode and cathode. Acta Mater 57(4):1165–1175

[5] Liu Q, Dong X, Xiao G, Zhao F, Chen F (2010) A novel electrode material for symmetrical SOFCs. Adv Mater 22(48):5478–5482

[6] Su C, Wang W, Liu M, Tadé MO, Shao Z (2015) Progress and prospects in symmetrical solid oxide fuel cells with two identical electrodes. Adv Energy Mater 5(14):1500188

[7] Wachsman ED, Lee KT (2011) Lowering the temperature of solid oxide fuel cells. Science 334(6058):935–939

[8] Ling Y, Yu J, Lin B, Zhang X, Zhao L, Liu X (2011) A cobalt-free $Sm_{0.5}Sr_{0.5}Fe_{0.8}Cu_{0.2}O_{3-\delta}$–$Ce_{0.8}Sm_{0.2}O_{2-\delta}$ composite cathode for proton-conducting solid oxide fuel cells. J Power Sources 198(5):2631–2634

[9] Ling Y, Chen H, Niu J, Wang F, Zhao L, Ou X, Nakamur T, Amezawa K (2016) Bismuth and indium co-doping strategy for developing stable and efficient barium zirconate-based proton conductors for high-performance H-SOFCs. J Eur Ceram Soc 36(14):3423–3431

[10] Fabbri E, Bi L, Pergolesi D, Traversa E (2012) Towards the next generation of solid oxide fuel cells operating below 600 °C with chemically stable proton-conducting electrolytes. Adv Mater 24(2):195–208

[11] An H, Lee H-W, Kim B-K, Son J-W, Yoon KJ, Kim H, Shin D, Ji H-I, Lee J-H (2018) A 5 × 5 cm^2 protonic ceramic fuel cell with a power density of 1.3 $W{\cdot}cm^{-2}$ at 600 °C. Nat Energy 3(10):870–875

[12] Duan C, Kee R, Zhu H, Sullivan N, Zhu L, Bian L, Jennings D, O'Hayre R (2019) Highly efficient reversible protonic ceramic electrochemical cells for power generation and fuel production. Nat Energy 4(3):230–240

[13] Wei K, Wang X, Zhu H, Liu H, Wang S, Chen F, Zhou F, Ling Y (2021) Clean and stable conversion of oxygen-bearing low-concentration coal mine gas by solid oxide fuel cells with an additional reforming layer. J Power Sources 506:230208

[14] Wei T, Qiu P, Jia L, Tan Y, Yang X, Sun S, Chen F, Li J (2020) Power and carbon monoxide co-production by a proton-conducting solid oxide fuel cell with $La_{0.6}Sr_{0.2}Cr_{0.85}Ni_{0.15}O_{3-\delta}$ for on-cell dry reforming of CH_4 by CO_2. J Mater Chem A 8(19):9806–9812

[15] Duan C, Kee RJ, Zhu H, Karakaya C, Chen Y, Ricote S, Jarry A, Crumlin EJ, Hook D, Braun R, Sullivan NP, O'Hayre R (2018) Highly durable, coking and sulfur tolerant, fuel-flexible protonic ceramic fuel cells. Nature 557(7704):217–222

[16.] Chen T, Wang WG, Miao H, Li T, Xu C (2011) Evaluation of carbon deposition behavior on the nickel/yttrium-stabilized zirconia anode-supported fuel cell fueled with simulated syngas. J Power Sources 196(5):2461–2468

[17] Authayanun S, Arpornwichanop A, Paengjuntuek W, Assabumrungrat S (2010) Thermodynamic study of hydrogen production from crude glycerol autothermal reforming for fuel cell applications. Int J Hydrogen Energ 35(13):6617–6623

[18] Steil MC, Nobrega SD, Georges S, Gelin P, Uhlenbruck S, Fonseca FC (2017) Durable direct ethanol anode-supported solid oxide fuel cell. Appl Energ 199:180–186

[19] Song W, Ma Z, Yang Y, Zhang S, Ou X, Ling Y (2020) Characterization and polarization DRT analysis of direct ethanol solid oxide fuel cells using low fuel partial pressures. Int J Hydrogen Energ 45(28):14480–14490

[20] Duan C, Tong J, Shang M, Nikodemski S, Sanders M, Ricote S, Almansoori A, O'Hayre R (2015) Readily processed protonic ceramic fuel cells with high performance at low temperatures. Science 349(6254):1321–1326

[21] Hua B, Yan N, Li M, Zhang YQ, Sun YF, Li J, Etsell T, Sarkar P, Chuang K, Luo JL (2016) Novel layered solid oxide fuel cells with multiple-twinned $Ni_{0.8}Co_{0.2}$ nanoparticles: the key to thermally independent CO_2 utilization and power-chemical cogeneration. Energ Environ Sci 9(1):207–215

[22] Hibino T, Hashimoto A, Suzuki M, Sano M (2002) A solid oxide fuel cell using Y-doped $BaCeO_3$ with Pd-Loaded FeO anode and $Ba_{0.5}Pr_{0.5}CoO_3$ cathode at low temperatures. J Electrochem Soc 149(11):A1503–A1508

[23] Nasani N, Wang Z-J, Willinger MG, Yaremchenko AA, Fagg DP (2014) In-situ redox cycling behaviour of Ni–$BaZr_{0.85}Y_{0.15}O_{3-\delta}$ cermet anodes for protonic ceramic fuel cells. Int J Hydrogen Energ 39(34):19780–19788

[24] An H, Shin D, Ji HI (2019) Effect of nickel addition on sintering behavior and electrical conductivity of $BaCe_{0.35}Zr_{0.5}Y_{0.15}O_{3-\delta}$. J Kor Ceram Soc 56(1):91–97

[25] Watenabe K, Yuasa M, Kida T, Teraoka Y, Yamazoe N, Shimanoe K (2010) High-performance oxygen-permeable membranes with an asymmetric structure using $Ba_{0.95}La_{0.05}FeO_{3-\delta}$ perovskite-type oxide. Adv Mater 22(21):2367–2370

[26] Chen C, Baiyee ZM, Ciucci F (2015) Unraveling the effect of la A-site substitution on oxygen ion diffusion and oxygen catalysis in perovskite $BaFeO_3$ by data-mining molecular dynamics and density functional theory. Phys Chem Chem Phys 17(37):24011–24019

[27] Tao Z, Bi L, Zhu Z, Liu W (2009) Novel cobalt-free cathode materials $BaCe_xFe_{1-x}O_{3-\delta}$ for proton-conducting solid oxide fuel cells. J Power Sources 194(2):801–804

[28] Cheng S, Wang Y, Zhuang L, Xue J, Wei Y, Feldhoff A, Caro J, Wang H (2016) A dual-phase ceramic membrane with extremely high H_2 permeation flux prepared by autoseparation of a ceramic precursor. Angewandte Chemie - Int Ed 55(36):10895–10898

[29] Zhong M, Feng Q, Yuan C, Liu X, Zhu B, Meng L, Zhou C, Xu J, Wang J, Rao G (2021) Photocurrent density and electrical properties of $Bi_{0.5}Na_{0.5}TiO_3$-$BaNi_{0.5}Nb_{0.5}O_3$ ceramics. J Adv Ceram. https://doi.org/10.1007/s40145-021-0497-7

[30] Du Z, Zhao H, Yi S, Xia Q, Gong Y, Zhang Y, Cheng X, Li Y, Gu L, Świerczek K (2016) High-performance anode material $Sr_2FeMo_{0.65}Ni_{0.35}O_{6-\delta}$ with In situ exsolved nanoparticle catalyst. ACS Nano 10(9):8660–8669

[31] Adijanto L, Padmanabhan VB, Kungas R, Gorte RJ, Vohs JM (2012) Transition metal-doped rare earth vanadates: a regenerable catalytic material for SOFC anodes. J Mater Chem 22(22):11396–11402

[32] Madsen BD, Kobsiriphat W, Wang Y, Marks LD, Barnett SA (2007) Nucleation of nanometer-scale electrocatalyst particles in solid oxide fuel cell anodes. J Power Sources 166(1):64–67

[33] Neagu D, Oh TS, Miller DN, Menard H, Bukhari SM, Gamble SR, Gorte RJ, Vohs JM, Irvine JTS (2015) Nano-socketed nickel particles with enhanced coking resistance grown in situ by redox exsolution. Nat Commun 6:8120

[34] Dong F, Ni M, He W, Chen Y, Yang G, Chen D, Shao Z (2016) An efficient electrocatalyst as cathode material for solid oxide fuel cells: $BaFe_{0.95}Sn_{0.05}O_{3-\delta}$. J Power Sources 326:459–465

[35] Dong F, Chen Y, Chen D, Shao Z (2014) Surprisingly high activity for oxygen reduction reaction of selected oxides lacking long oxygen-ion diffusion paths at intermediate temperatures: a case study of cobalt-free $BaFeO_{3-\delta}$. Acs Appl Mater Inter 6(14):11180–11189

[36] Niu B, Jin F, Feng T, Zhang L, Zhang Y, He T (2018) A-site deficient $(La_{0.6}Sr_{0.4})_{(1-x)}Co_{0.2}Fe_{0.6}Nb_{0.2}O_{3-\delta}$ symmetrical electrode materials for solid oxide fuel cells. Electrochim Acta 270:174–182

[37] Markov AA, Patrakeev MV, Savinskaya OA, Nemudry AP, Leonidov IA, Leonidova ON, Kozhevnikov VL (2008) Oxygen nonstoichiometry and high-temperature transport in $SrFe_{1-x}W_xO_{3-\delta}$. Solid State Ionics 179(1):99–103

[38] Li P, Yang W, Tian C, Zhao W, Lü Z, Xie Z, Wang C-A (2021) Electrochemical performance of $La_2NiO_{4+\delta}$-$Ce_{0.55}La_{0.45}O_{2-\delta}$ as a promising bifunctional oxygen electrode for reversible solid oxide cells. J Adv Ceram 10(2):328–337

[39] Escudero MJ, Aguadero A, Alonso JA, Daza L (2007) A kinetic study of oxygen reduction reaction on La_2NiO_4 cathodes by means of impedance spectroscopy. J Electroanal Chem 611(1):107–116

[40] Adler SB (1998) Mechanism and kinetics of oxygen reduction on porous $La_{1-x}Sr_xCoO_{3-\delta}$ electrodes. Solid State Ionics 111(1):125–134

[41] Hou J, Wang Q, Li J, Lu Y, Wang L, Fu XZ, Luo JL (2020) Rational design of an in-situ co-assembly nanocomposite cathode $La_{0.5}Sr_{1.5}MnO_{4+\delta}$-$La_{0.5}Sr_{0.5}MnO_{3-\delta}$ for lower-temperature proton-conducting solid oxide fuel cells. J Power Sources 466:228240

[42] Shi N, Su F, Huan D, Xie Y, Lin J, Tan W, Peng R, Xia C, Chen C, Lu Y (2017) Performance and DRT analysis of P-SOFCs fabricated using new phase inversion combined tape casting technology. J Mater Chem A 5(37):19664–19671

[43] Xia J, Wang C, Wang X, Bi L, Zhang Y (2020) A perspective on DRT applications for the analysis of solid oxide cell electrodes. Electrochim Acta 349:136328

[44] Wang X, Ma Z, Zhang T, Kang J, Ou X, Feng P, Wang S, Zhou F, Ling Y (2018) Charge-transfer modeling and polarization DRT analysis of proton ceramics fuel cells based on mixed conductive electrolyte with the modified anode-electrolyte interface. Acs Appl Mater Inter 10(41):35047–35059

[45] Yang Y, Bao H, Ni H, Ou X, Wang S, Lin B, Feng P, Ling Y (2021) A novel facile strategy to suppress Sr segregation for high-entropy stabilized $La_{0.8}Sr_{0.2}MnO_{3-delta}$ cathode. J Power Sources 482:228959